Astronomy & Astrophysics manuscript no. output
July 4, 2023

The β Pictoris b Hill Sphere Transit Campaign

II. Searching for the signatures of the β Pictoris exoplanets through time delay analysis of the δ Scuti pulsations

Sebastian Zieba[1,2,3], Konstanze Zwintz[3], Matthew Kenworthy[2], Daniel Hey[4], Simon J. Murphy[5], Rainer Kuschnig[6], Lyu Abe[7], Abdelkrim Agabi[7], Djamel Mekarnia[7], Tristan Guillot[7], François-Xavier Schmider[7], Philippe Stee[7], Yuri De Pra[8], Marco Buttu[9,10], Nicolas Crouzet[2], Samuel Mellon[11], Jeb Bailey III[12], Remko Stuik[2], Patrick Dorval[13], Geert-Jan J. Talens[14], Steven Crawford[15], Eric Mamajek[10,16], Iva Laginja[17], Michael Ireland[18], Blaine Lomberg[19,20], Rudi Kuhn[19], Ignas Snellen[2], Paul Kalas[22,23,24], Jason J. Wang[25], Kevin B. Stevenson[26], Ernst de Mooij[27,28], Anne-Marie Lagrange[29,30,31], Sylvestre Lacour[17], A. Lecavelier des Etangs[30], Mathias Nowak[31], Paul A. Strøm[32,33], Z. Hui[34], and L. Wang[35]

(Affiliations can be found after the references)

Received July 4, 2023; accepted —

ABSTRACT

Context. The β Pictoris system is the closest known stellar system with directly detected gas giant planets, an edge-on circumstellar disk, and evidence for falling sublimating bodies and transiting exocomets. The inner planet, β Pictoris c, is also indirectly detected with radial velocity measurements. The star is a known δ Scuti pulsator, and the long term stability of these pulsations opens up the possibility of indirectly detecting the gas giant planets through time delays of these pulsations due to a varying light travel time.

Aims. We search for phase shifts in the δ Scuti pulsations consistent with the known planets β Pictoris b and c and carry out an analysis of the stellar pulsations of β Pictoris over a multi-year timescale.

Methods. We use photometric data collected by the BRITE-Constellation, bRing, ASTEP and TESS to derive a list of the strongest significant δ Scuti pulsations. We carry out an analysis with the open-source python package `maelstrom` to study the stability of the pulsation modes of β Pictoris to determine the long term trends in the pulsations seen.

Results. We do not detect the expected signal for β Pictoris b or β Pictoris c. The expected time delay is 6 seconds for β Pictoris c and 24 seconds for β Pictoris b. With simulations we determine that the photometric noise in all the combined data sets cannot reach the sensitivity needed to detect the expected timing drifts. An analysis of the pulsational modes of β Pictoris using `maelstrom` shows that the modes themselves drift on the timescale of a year, fundamentally limiting our ability to detect exoplanets around β Pictoris via pulsation timing.

Conclusions.

Key words. Asteroseismology

1. Introduction

β Pictoris is a nearby, southern hemisphere star visible by naked eye for which δ Scuti -like pulsations were discovered by Koen (2003). The planetary-mass companion β Pictoris b was detected using the VLT/NaCo instrument with direct imaging (Lagrange et al. 2009b, 2010). Evidence of a second planet in the β Pictoris system was published by Lagrange et al. (2019b) using the radial-velocity method and recently independently confirmed by Nowak et al. (2020) and Lagrange et al. (2020) using VLTI/GRAVITY observations.

The lifetime and frequency stability of δ Scuti pulsations make them astronomical "stellar clocks" and therefore great targets for applying timing techniques (Compton et al. 2016). The common orbital motion of the star together with a companion around the barycenter of the system results in a periodic early or late arrival of the signals. This principle led to the first detection of planets outside our solar system orbiting a pulsar (Wolszczan & Frail 1992; Wolszczan 1994). This periodic variation of the arrival times can be either seen as a frequency modulation (FM; Shibahashi & Kurtz 2012; Shibahashi et al. 2015) or phase modulation (PM; Murphy et al. 2014; Murphy & Shibahashi 2015; Murphy et al. 2016b). The latter method works better for companions in wider orbits.

Applying the PM method on Kepler data, Murphy et al. (2016a) discovered a massive planet ($m \sin i \approx 12 M_J$) with an orbital period of about 840 days around a δ Scuti star. In addition to the discovery of this planet, the PM method has led to the detection of 341 binaries and hundreds more candidates (Murphy et al. 2018). It furthermore provides us with the eccentricity, period and mass function of the companion, just like the radial velocity (RV) method does (e.g. Nesvold & Kuchner 2015).

Applying the same method on pulsating stars observed by the TESS mission will lead to many more binary systems with full orbital solutions. β Pictoris was observed for approximately four months from October 2018 to February 2019 during the primary mission of TESS. A second visit occurred during TESS' extended mission from November 2020 to February 2021 (see Table 3 for a summary of all visits).

We use the data collected by the TESS satellite in its primary mission and data collected by the Hill sphere[1] transit

---

[1] The Hill sphere is the region around a planet where masses - like moons and planetary rings - are gravitationally bound to it.

campaign, which was an international effort of space-based (e.g. through the BRITE-Constellation) and ground-based (e.g. through bRing, ASTEP) observations in order to search for signatures of material around the giant planet β Pictoris b (Kalas et al. 2019; Kenworthy 2017). In this work, we will analyze this photometric data by searching for phase variations (and therefore time delays) caused by orbital motion in the pulsational signals.

In Section 2 we describe the properties of the different components in the β Pictoris system. Section 3 has a summary of all observational instruments and a frequency analysis for the photometry collected by TESS. The theory and equations for this paper can be found in Section 4, and our results and conclusions follow in Sections 5 and 6.

2. The β Pictoris System

β Pictoris (HD 39060; HR 2020) is one of the most studied and intriguing star-planet systems. The Infrared Astronomical Satellite (IRAS) discovered an infrared excess (Aumann et al. 1984) for this bright and close southern star, which was attributed to the presence of a circumstellar disk. This disk was first imaged by Smith & Terrile (1984) and clearly showed the edge-on geometry of this system. The gas and dust in this disk is mostly "second generation", i.e. constantly replenished by collisions of comets and asteroids (Lagrange et al. 2000). A warp in this disk (Augereau et al. 2001; Mouillet et al. 1997; Nesvold & Kuchner 2015) and signatures of evaporating exocomets (also called Falling Evaporating Bodies or FEBs) in spectroscopy (Ferlet et al. 1987; Beust & Morbidelli 2000) were attributed to an exoplanet orbiting the star interacting dynamically with its environment.

2.1. The star

Koen (2003) discovered δ Scuti type pulsations at the millimagnitude level originating from β Pictoris. Further analysis by Mékarnia et al. (2017), Zwintz et al. (2019) and Zieba et al. (2019) showed dozens of additional frequencies between 20 and 80 cycles per day. Those pulsations also induce intrinsic variations in the radial velocity at $\lesssim 1$ km s^{-1} peak-to-peak (Lagrange et al. 2009a, 2012; Galland et al. 2006) which hampers the search for planets with the radial velocity method in this system. A selection of fundamental properties of the star β Pictoris are listed in Table 1.

Table 1. Various stellar parameters of the star β Pictoris.

Parameter	Value	Reference
RA (J2000.0)	05h 47m 17.09s	1
DEC (J2000.0)	-51h 03m 59.41s	1
V (mag)	3.86	2
TESS (mag)	3.696	1
age (Myr)	23 ± 3	3
parallax (mas)	50.93 ± 0.15	4,5,6
Distance (pc)	19.63 ± 0.06	4,5,6
Spectral class	A6V	7
Radius ($R_\odot$)	1.497 ± 0.025	8
Mass ($M_\odot$)	$1.75^{+0.03}_{-0.02}$	9
Teff (K)	8090 ± 59	8

References. (1) Stassun et al. (2019); (2) Cousins (1971); (3) Mamajek & Bell (2014); (4) Gaia Collaboration et al. (2016); (5) Gaia Collaboration et al. (2023); (6) Lindegren et al. (2021); (7) Gray et al. (2006); (8) Zwintz et al. (2019); (9) Lacour et al. (2021).

2.2. The planets: β Pictoris b and c

The warp of the inner disk of β Pictoris observed in 1998 by the Hubble Space telescope was one of the indirect lines of evidence for a massive substellar companion orbiting the star. Signatures of infalling exocomets in the spectra of the star also needed a "perturber" to scatter them onto eccentric inner system bearing orbits. The planet, β Pictoris b, was then discovered using the VLT/NaCo instrument data in 2003 (Lagrange et al. 2009b) and was later confirmed by Lagrange et al. (2010). A transit-like event has also been observed in 1981 and attributed to a planet (Lecavelier Des Etangs et al. 1995) however, a better orbit determination with the VLT/SPHERE instrument ruled out β Pictoris b as the cause for it (Lagrange et al. 2019a). Furthermore, using data from the Gemini Planet Imager, Wang et al. (2016) were able to rule out a transit of the planet β Pictoris b during the conjunction in 2017 at a 10σ level. However, a Hill sphere transit was predicted for the time between late 2017 and early 2018 (Lecavelier des Etangs & Vidal-Madjar 2016; Wang et al. 2016). Various observational campaigns were initiated by e.g. PicSat (Nowak et al. 2018; Menegaldo et al. 2022), bRing (Kenworthy 2017) and the BRITE constellation (Weiss et al. 2014) in order to photometrically observe possible material around the planet; however without any significant detection (Kenworthy et al. 2021). The mass and the orbital solution of the outer planet β Pictoris b are listed in Table 2.

Table 2. Various parameters of the planets β Pictoris b and c based on Lacour et al. (2021).

Parameter	Unit	β Pictoris b	β Pictoris c
Mass	M_J	$11.90^{+2.93}_{-3.04}$	$8.89^{+0.75}_{-0.75}$
a	au	$9.93^{+0.03}_{-0.03}$	$2.68^{+0.02}_{-0.02}$
e	—	$0.103^{+0.003}_{-0.003}$	$0.32^{+0.02}_{-0.02}$
i	°	$89.00^{+0.00}_{-0.01}$	$88.95^{+0.09}_{-0.10}$
$\varpi^{(a)}$	°	$199.3^{+2.8}_{-3.1}$	$66.0^{+1.8}_{-1.7}$
$\tau^{(b)}$	—	$0.719^{+0.008}_{-0.010}$	$0.724^{+0.006}_{-0.006}$
P	years	$23.61^{+0.09}_{-0.09}$	3.34 ± 0.04
P	days	8623^{+31}_{-32}	1221 ± 15
$t_p{}^{(c)}$	MJD	65243	59888

Notes.

[a] The argument of periastron ϖ reported in Lacour et al. (2021) follows the definition in Blunt et al. (2020) and therefore refers to the orbit of the companion and not to the star. In this paper, however, we refer to the orbit of the star when we use ϖ.

[b] reference epoch MJD 59000 (31 May 2020).

[c] derived from τ.

Evidence of an additional planet in the β Pictoris system was published by Lagrange et al. (2019b). Over 6000 spectra of the star taken between 2003 and 2018 by the HARPS instrument at the ESO La Silla 3.6 m telescope have been analyzed and showed a hint of a planetary signal. β Pictoris c was then ultimately directly detected by Nowak et al. (2020) and Lagrange et al. (2020) using VLTI/GRAVITY observations. A list of parameters for the planet can be found in Table 2.

3. Observations

Due to the 2017-2018 Hill Sphere Transit of β Pictoris b, an international campaign of space and ground-based observations was launched in order to search for signatures of material around the giant planet (Kalas et al. 2019; Kenworthy et al. 2021). Table 3 summarizes various properties of the different light curves. Changes to those light curves other than the Gaussian high-pass procedure - which is explained in Section A.2 - are noted in the following subsections. The data provided by BRITE-Constellation was left unchanged. A detailed analysis of the photometry of β Pictoris collected by BRITE-Constellation and bRing was published by Zwintz et al. (2019). As we want to measure the periodic motion of a star around a barycenter, we also want to correct for the motion of our earth in our solar system. All the observations in this work were therefore converted to the Barycentric Julian Date in the Barycentric Dynamical Time (BJD$_{\rm TBD}$) standard using the `Python` tool `BARYCORRPY` (Kanodia & Wright 2018) which is based on the IDL code `BARYCORR` (Wright & Eastman 2014).

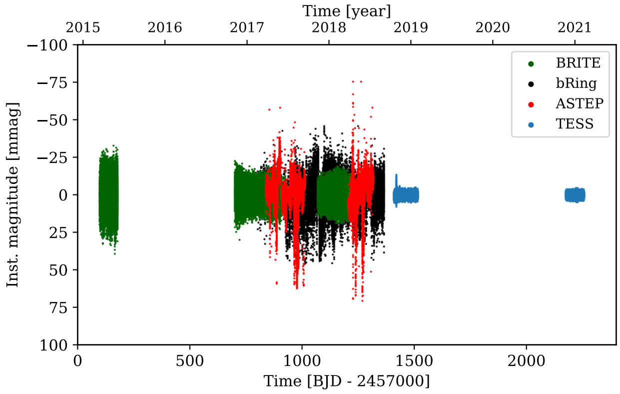

Fig. 1. The full light curve of all available observations of the star β Pictoris used in this work.

3.1. BRITE-Constellation

The BRITE-Constellation (Weiss et al. 2014) consists of five nanosatellites collecting photometry for the brightest stars on the sky. In this work, we analyzed data collected by three of the satellites: BRITE-Heweliusz (BHr), BRITE-Toronto (BTr), BRITE-Lem (BLb). Being in a low-earth orbit the orbital periods of the satellites are all around 100 minutes. A minimum of 15 minutes per orbit are dedicated to observations. Three different runs were conducted in the constellations around Pictor and Vela which also included the star β Pictoris. A summary of the durations and various properties of those observations can be found in Table 3. The pipeline for the photometry reduction is described in Popowicz et al. (2017). An analysis of all BRITE observations was conducted in Zwintz et al. (2019). For the three runs by BHr, BTr+BHr and BHr, which all used the red BRITE filter, 6, 13 and 8 significant frequencies were extracted, respectively. The only run with a blue filter by BLb suffered from higher noise compared to the other BRITE-observations. Zwintz et al. (2019) report four frequencies in the collected BLb photometry. The blue observations were discarded from this analysis as the data quality is not good enough to provide additional information.

3.2. bRing

bRing, standing for “the β Pictoris b Ring project”, was initiated in order to collect photometry of β Pictoris during the Hill sphere transit of β Pictoris b at the end of 2017 (Stuik et al. 2017). For that, two stations in South Africa and Australia were built, each consisting of two wide-field cameras. Their design is based on the Multi-Site All-Sky CAmeRA (MASCARA) (Snellen et al. 2012; Talens et al. 2017). The capability of bRing to monitor bright stars and to find previously unknown variables was shown by Mellon et al. (2019). More information on the observing strategy and design of bRing can be found in Stuik et al. (2017). The reduction pipeline for the MASCARA and bRing instruments is described in Talens et al. (2018). With a passband of 463 - 639 nm, bRing collected the shortest wavelengths of all observatories considered in this work. We expect to see the highest pulsational amplitudes in these data as β Pictoris is a star of spectral type A6 (Zwintz et al. 2019) which has its energy maximum in the blue optical wavelengths.

Due to some evident outliers in the data, one 5σ clip with respect to the median of the dataset was applied. This significantly weakens the one-day aliases in the spectral window. An iterative sigma clipping procedure was not conducted due to noticeable changes in the amplitudes of the pulsations in this case (see Hogg et al. (2010) for a discussion of sigma clipping in order to remove outliers). The observations by bRing were separated into two equally sized segments to gain more time delay measurements while keeping a precision in frequency and phase comparable to the ASTEP observations. Zwintz et al. (2019) found six significant frequencies in the photometry collected by bRing. All of them are also identified in the data collected by BRITE, ASTEP and TESS.

3.3. ASTEP

ASTEP, standing for the Antartica Search for Transiting Extrasolar Planets, is an automated telescope with an aperture of 40 cm located at the Concordia station at Dome C in Antarctica (Abe et al. 2013; Guillot et al. 2015; Mékarnia et al. 2017). It uses a Sloan i’ filter (centered at 763 nm).

Only measurements with a sun elevation lower than -18° were used. Furthermore, datapoints where the centroid of the star did not not fall on the central pixel suffer from strong outliers. The removal of those and a 5-σ clip with respect the median weakens aliases significantly without noticeable changes in the amplitude of the strongest pulsational frequencies. Mékarnia et al. (2017) conduced a frequency analysis of the β Pictoris photometry collected by the ASTEP observatory and are consistent with the ones seen in the TESS data.

3.4. TESS

The Transiting Exoplanet Survey Satellite (TESS; Ricker et al. 2015) was launched in April 2018 in order to find transiting exoplanets around nearby, bright stars. The data of β Pictoris (TIC 270577175, T = 3.696 mag) was collected from 19 October 2018 to 1 February 2019 in the sectors 4 through 7 and from 20 November 2020 to 8 February 2021 in the sectors 32 through 34. The first four sectors were taken during TESS’ primary mission and the three other approximately two years later

Table 3. A summary of the properties of the various instruments and corresponding light curves: T denotes the timebase of the observations, the reciprocal value $1/T$ corresponds to the Rayleigh criterion. $f_{\mathrm{Ny.}}$ is the Nyquist frequency and DC the duty cycle.

Observation	Wavelength (nm)	Observation start	Observation end	T (days)	$1/T$ (10^{-3} d^{-1})	$f_{\mathrm{Ny.}}$ (d^{-1})	cadence (s)	DC (%)
BHr	550 - 700	16 March 2015	2 June 2015	78.32	12.77	4167	10.37	6.78
BTr + BHr	550 - 700	4 Nov. 2016	17 June 2017	224.6	4.453	2128	20.30	7.07
BHr	550 - 700	9 Nov. 2017	25 April 2018	167.3	5.976	2128	20.30	7.48
bRing	463 - 639	2 Feb. 2017	1 Sept. 2018	575.5	1.738	135.4	319.1	27.0
ASTEP17	695 - 844	28 March 2017	14 Sept. 2017	170.0	5.881	495.8	87.13	18.9
ASTEP18	695 - 844	28 March 2018	15 July 2018	109.3	9.150	502.8	85.92	29.2
TESS	600 - 1000	19 Oct. 2018	1 Feb. 2019	105.2	9.507	360.0	120.0	85.3
TESS	600 - 1000	20 Nov. 2020	8 Feb. 2021	79.8	12.53	360.0	120.0	90.2

BRITE Lem (BLb) - is equipped with a blue filter and observed β Pictoris from December 2016 until June 2017 but due to significantly higher noise in the time series, the data was regarded from the analysis. See Zwintz et al. (2019) for an analysis of the BLb observations.

as part of the first extended mission. β Pictoris is one of the preselected targets for which short cadence (2 minute) data are provided. Due to this high cadence data, the high photometric precision of TESS, its high duty cycle and the long baseline, δ Scuti pulsations can be resolved and identified to a high precision. The photometric data of β Pictoris as observed by TESS was accessed and modified with the Python package `lightkurve` (Lightkurve Collaboration et al. 2018), which retrieves the data from the MAST archive[2]. For this analysis we used the Presearch Data Conditioning Simple Aperture Photometry (PDCSAP; Smith et al. 2012; Stumpe et al. 2012) light curves which are produced from the Science Processing Operations Center (SPOC) pipeline (Jenkins et al. 2016; Jenkins 2017; Jenkins et al. 2010). These PDCSAP light curves were corrected for systematics by the SPOC pipeline. We also visually inspected the Target Pixel Files (TPF) in order to rule out various instrumental and astrophysical effects like for example solar system asteroids or comets crossing the field of view. A comparison of the Lomb Scargle periodogram (Lomb 1976; Scargle 1982) of the raw SAP and PDCSAP light curves shows a significant change in the noise at low frequencies. This is due to the systematic effects present in sector 4. The lowest noise in the low frequency range can be found for the PDCSAP light curve with a completely removed fourth sector. This light curve was then used for the main frequency analysis.

The individual sectors were normalized by dividing each of the sectors by their respective median flux and combined into one light curve. Furthermore, every measurement with a nonzero quality flag (see Sect. 9 in the TESS Science Data Products Description Document)[3] was removed. They mark anomalies like cosmic ray events or instrumental issues.

The frequency analysis was conducted using the Python package `SMURFS` (Müllner 2020) and checked with the software package `Period04` (Lenz & Breger 2005). All pulsation frequencies down to a signal to noise ratio of 4 following Breger et al. (1993) were extracted. The frequency range analysed is between 0 and the Nyquist frequency of 360 cycles per day. Following the procedure described in Zieba et al. (2019), 37 significant p-modes in the frequency range from 34 to 76 d^{-1} were identified. As we are only interested in the strongest pulsational frequencies for this time delay analysis, we did not further tried to recover any of the lower amplitude modes. A list of the extracted frequencies can be found in Table A.1.

4. Theory and Methodology

In this chapter we discuss the theory behind time delays and the methods used in order to finally arrive at the time delay plot which can be used to search for companions around pulsating stars.

4.1. δ Scuti stars

δ Scuti stars can be found at the intersection region between the main-sequence and the instability strip on the Hertzsprung-Russel diagram. Thanks to the nearly uninterrupted, high-precision photometry of Kepler's primary four year mission, our understanding of pulsating stars has been revolutionized. δ Scuti stars have masses between approximately 1.5 and 2.5 $M_\odot$. They pulsate in radial and non-radial, low-degree, low-order, pressure (p) modes that are primarily driven by an opacity mechanism (also called κ-mechanism) in their HeII zone with contributions from turbulent pressure (Houdek 2000; Antoci et al. 2014) and the edge-bump mechanism (Murphy et al. 2020). Those oscillations have periods between 18 minutes and 8 hours, respectively 3 and 80 cycles per day (Aerts et al. 2010). Linear combinations of those oscillations can however create peaks at lower frequencies (Breger & Montgomery 2014). Besides main-sequence and more evolved stars, δ Scuti pulsations were observed in pre-main-sequence stars, thus giving us the possibility to learn about early stellar evolution (Zwintz et al. 2014; Murphy et al. 2021; Steindl et al. 2022).

4.2. The ephemeris equation

The search for time delays in certain astrophysical signals requires a (quasi-)periodic process in space. A review on this and the related equations can be found in Hermes (2018). There are different processes which are "clock-like" under the assumption of a closed system: the exceptionally stable signals of pulsars, the eclipse time of binary stars or certain pulsating stars as in our case. Deviations from a periodic signals can be used to analyse the spin down of pulsars or to discover companions around pulsars (Wolszczan & Frail 1992; Wolszczan 1994), eclipsing binaries (Barnes & Moffett 1975) or pulsating stars (Silvotti et al. 2007) (for a general review of pulsating stars in binary sys-

---

[2] https://archive.stsci.edu/tess/

[3] https://archive.stsci.edu/missions/tess/doc/EXP-TESS-ARC-ICD-TM-0014.pdf

tems see Murphy 2018). This is done by creating O-C (observed minus calculated) diagrams (see e.g. Sterken 2005) in order to search for deviations from the predicted ephemeris in the observations. O-C diagrams work the best if the star is pulsating in only a single mode and if the maxima are narrow and well defined – they are easy to track in that case. They struggle however especially with multi-mode pulsators.

4.3. Frequency modulation and Phase modulation: state-of-the-art

Building on those established methods of O-C diagrams two new and complementary techniques arose in order to find companions around pulsating stars. The FM method (Shibahashi & Kurtz 2012) searches and analyses the variations in the frequency of the pulsating star induced by a companion. The periodic frequency modulation creates multiples around every pulsation peak in the frequency spectrum. Their frequencies, relative amplitudes and phases can be used to get the full orbital solution as described in Shibahashi et al. (2015). Its effectiveness was validated by comparison with a eclipsing binary system (Kurtz et al. 2015). The FM method is best suited for data sets with a baseline which exceeds the orbital period of the companion.

The PM method is more sensitive to companions in wider orbits and was developed by Murphy et al. (2014), Murphy & Shibahashi (2015), and Murphy et al. (2016b). Compton et al. (2016) showed that δ Scuti stars and white dwarfs are best suited for this method. Its effectiveness was demonstrated by Schmid et al. (2015) by showing the binary nature of KIC10080943 using the PM method and attributing certain pulsations to the corresponding star in the binary due to the antiphase modulation in the time delays. Such a system with observable time delays in both components is called PB2, analagous to spectroscopic terminology, where binary star systems are called SB2s if both stars show observable radial velocities. Other proof of the functionality of the PM method was shown by Derekas et al. (2019) by comparing the orbital parameters derived from RV with those from PM.

An additional advantage of the PM method is its easier automation for many stars. Applying this method on 2224 main-sequence A/F stars in the 4-year main Kepler data, Murphy et al. (2018) were able to find 317 PB1 systems, where only one component is pulsating and showing time delays, and 24 PB2 systems, where two stars are pulsating. It is worth noting here that determining orbital solutions using spectra and generating radial velocity curves for the same number of stars would be much more time intensive.

Other methods were developed by Koen (2014) and Balona (2014) to search for binary systems by tracing the δ Scuti pulsations of stars. They are not able however, in contrast to the FM and PM method, to provide a full orbital solution which is usually gained by analysing radial velocity (RV) curves of spectroscopic binaries.

4.4. Time Delays

Time delays arise when a signal (in our case always an electromagnetic wave with the propagation velocity defined by the speed of light) has to travel different distances at different epochs. Following Smart (1977) and Balona (2014), the distance r between the pulsating star and the center of gravity of its system can be described by

$$r = \frac{a_1\left(1-e^2\right)}{1+e\cos f} \tag{1}$$

where a_1 denotes the major-semi axis of the star, e its eccentricity and f the true anomaly. The distance to the star varies relative to the earth by

$$z = r\sin(f+\varpi)\sin i \tag{2}$$

with ϖ being the the argument of periapsis, i.e. the angle between the nodal point and the periapsis[4] and i the inclination of the system.

We can now substitute Equation 1 into Equation 2. The time delay $\tau = -z/c$ is then completely described by the following equation:

$$\tau(t,\mathbf{x}) = -\frac{a_1\sin i}{c}(1-e^2)\frac{\sin f\cos\varpi + \cos f\sin\varpi}{1+e\cos f}. \tag{3}$$

The set $\mathbf{x} = (\Omega = 2\pi/P, a_1\sin i/c, e, \varpi, t_p)$ in Equation 3 includes all system specific parameters which are needed to describe the time delay for a given time t. P is the orbital period of the system, or equivalently $1/P = \nu_{\mathrm{orb}}$ the orbital frequency and thus Ω the angular orbital frequency. The projected semi-major axis of the pulsating star is described by $a_1\sin i$. Dividing this quantity by the speed of light c gives us the size of the orbit for the pulsating star in light seconds. The argument of periapsis is described by ϖ and the time of periapsis passage by t_p. For a graphical visualisation of the orbital parameters see Murphy & Shibahashi (2015).

The two trigonometric functions of the true anomaly, $\sin f$ and $\cos f$, can be expressed in terms of series expansions and Bessel functions:

$$\cos f = -e + \frac{2\left(1-e^2\right)}{e}\sum_{n=1}^{\infty} J_n(ne)\cos n\Omega\left(t-t_{\mathrm{p}}\right) \tag{4}$$

$$\sin f = 2\sqrt{1-e^2}\sum_{n=1}^{\infty} J_n'(ne)\sin n\Omega\left(t-t_{\mathrm{p}}\right) \tag{5}$$

with $J_n'(x) = \mathrm{d}J_n(x)/\mathrm{d}x$ (the derivation of Equation 4 and 5 can be found in Appendix A of Shibahashi et al. 2015). The changing distances between us and the clock in space are fundamentally connected with varying radial velocities, v_{rad} :

$$v_{\mathrm{rad}} = c\frac{\mathrm{d}\tau}{\mathrm{d}t}. \tag{6}$$

Substituting Equation 3 into Equation 6 gives us:

$$v_{\mathrm{rad}} = -\frac{\Omega a_1\sin i}{\sqrt{1-e^2}}[\cos(f+\varpi) + e\cos\varpi], \tag{7}$$

---

[4] The argument of periapsis is usually denoted with ω. The latter symbol is however used in asteroseismology to denote the angular oscillation frequency. One should also not confuse ϖ with the longitude of periapsis which is the sum of the longitude of the ascending node Ω and the argument of periapsis.

Given Equation 6 and the convention that a positive radial velocity corresponds with an receding object and a negative with an approaching one, we can deduce the following: a negative time delay is due to an early arrival of the signal, i.e. the star is closer to us and vice versa[5] (see Table 4).

Table 4. Sign convention for the radial velocity $v_{\rm rad}$ and the time delays τ.

	positive sign (+)	negative sign (-)
$v_{\rm rad}$	moving away	approaching
τ	further away / late arrival	closer / early arrival

We see in Equation 3 and 7 that the time delay as well as the radial velocity of a system can be completely described by the orbital parameters. If we obtain those parameters by one method we can predict what we should observe with the other one. Furthermore, if we generate the time delay plot from our observations, we can apply a chi-squared minimization technique in order to get the parameters in set **x**. This concept was introduced with Murphy & Shibahashi (2015) and is a major improvement to Murphy et al. (2014) where the time delay measurements were numerically differentiated in order to derive the parameters from the obtained radial velocity curve.

Finally, by using two of the derived orbital parameters, $a_1 \sin i/c$ and $P_{\rm orb}$, we can calculate the mass function $f(m_1, m_2, \sin i)$ for the binary system:

$$f(m_1, m_2, \sin i) := \frac{(m_2 \sin i)^3}{(m_1 + m_2)^2} = \frac{4\pi^2 c^3}{G} v_{\rm orb}^2 \left(\frac{a_1 \sin i}{c}\right)^3 \tag{8}$$

with m_2 being the mass of the (usually non-pulsating) companion and G the gravitational constant.

4.5. Phase Modulation Method: Methodology

Before we can create the time delay plot, we have to analyse the change in phase of the various pulsation modes with time. The basic equations for that can be found in Murphy et al. (2014) and are summarized in the following. We start by dividing the light curve in n equally sized segments. Then, we calculate the phase in every segment for each frequency. This leaves us with a series of phases Φ_j for every segment $(1, 2, \ldots, n)$ for a fixed frequency ν_j:

$$\Phi_j = \left[\phi_{1j}, \phi_{2j}, \ldots, \phi_{ij}, \ldots, \phi_{nj}\right] \tag{9}$$

Numerically, the phase in a segment is derived by calculating the argument of the Fourier Transformation in the respective segment:

$$\Phi(t;\nu) = \tan^{-1}\left(\frac{\mathrm{Im}(\mathrm{F}(t;\nu,\delta t))}{\mathrm{Real}(\mathrm{F}(t;\nu,\delta t))}\right), \tag{10}$$

where $\mathrm{F}(t;\nu,\delta t)$ is the value of the Fourier Transformation of the time series for frequency ν in segment δt.

As phases are frequency dependent, the resulting phase shifts will have different amplitudes for different frequencies. To get rid of this effect we convert them into time delays by first calculating the relative phase shifts:

$$\Delta\phi_{ij} = \phi_{ij} - \overline{\phi}_j, \tag{11}$$

with $\overline{\phi}_j$ being the mean phase of frequency ν_j:

$$\overline{\phi}_j = \frac{1}{n}\sum_{i=1}^{n} \phi_{ij} \tag{12}$$

The time delay τ_{ij} for segment i and frequency ν_j is then simply the relative phase shift divided by the angular pulsation frequency:

$$\tau_{ij} = \frac{\Delta\phi_{ij}}{2\pi\nu_j} \tag{13}$$

A planet with a orbital frequency of $\nu_{\rm orb}$ in a circular orbit will induce time delays which can be described by a sine function with phase ψ:

$$\tau(t) = A \sin(2\pi\nu_{\rm orb} t + \psi) \tag{14}$$

The amplitude A can be simply derived by inserting the center of mass equation $m_1 a_1 = m_2 a_2$ in $\tau = a_1 \sin i/c$:

$$\tau = \frac{a_{\rm P} \sin i}{c} \frac{M_{\rm S}}{M_*} \tag{15}$$

with $a_{\rm S}$ being the major semi axis of the companion. $M_{\rm S}$ and M_* being the mass of the companion and the star, respectively. Using Equation 15 and the mass of around 1.8 $M_\odot$ given in Table 1 we can calculate the expected time delay for a given period. This is visualised in Figure 2. The time delay is around 24 seconds for β Pictoris b and 6 seconds for β Pictoris c. For comparison, the smallest TD detected in the main Kepler data is 7 seconds (Murphy et al. 2016a).

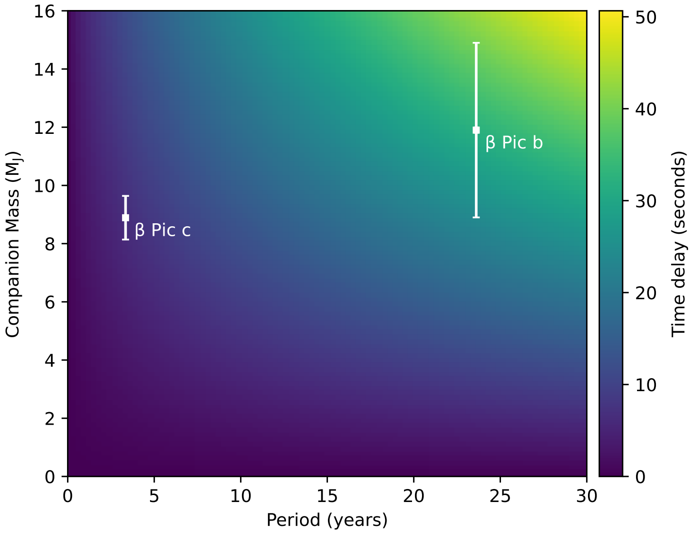

Fig. 2. Time delays for the β Pictoris system. The colors indicate the expected time delays for an edge-on planet on a circular orbit. The uncertainties in the orbital period for the planets are smaller than the marker size.

---

[5] This convention for the time delays was established with Murphy & Shibahashi (2015), whilst Murphy et al. (2014) used reversed signs and their plots are reflected in the vertical axis.

For more eccentric orbits, the pulsation time plot will be described by a sum of harmonics with amplitudes A_k and phases ϕ_k corresponding to order k:

$$\tau(t) = \sum_{k=1}^{N} A_k \sin\left(2\pi k \nu_{\rm orb} t + \psi_k\right) \tag{16}$$

The height of the first harmonic relative to the one of the orbital frequency is a measure of the eccentricity. The theory behind this is described in Appendix A of Murphy et al. (2014). A visualization of that can be seen in Figure 3. An increase in eccentricity also influences the amplitude of the time delay. This is given by the following equation:

$$\frac{a_1 \sin i}{c} = \frac{(\tau_{\rm max} - \tau_{\rm min})}{2} \left(1 - e^2 \cos^2 \varpi\right)^{-1/2}. \tag{17}$$

The maximum time delay is therefore reached in the case of $\varpi = \pm\pi/2$ or for the simple circular orbit case.

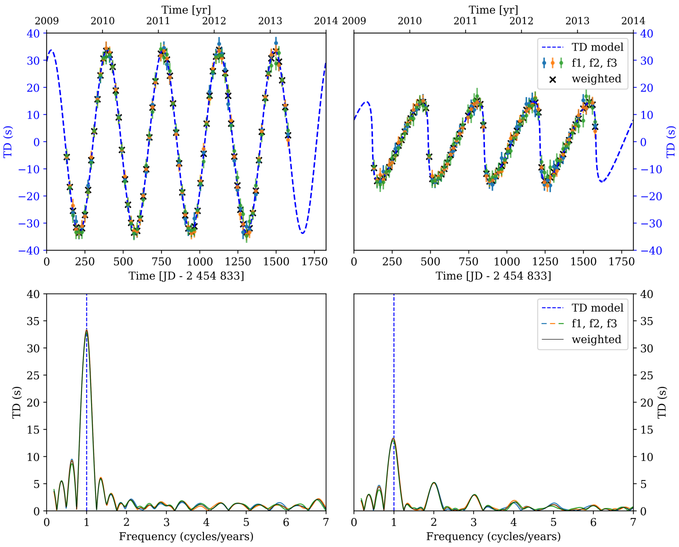

Fig. 3. Simulation of a companion in a circular ($e = 0$; left column) and eccentric ($e = 0.9$; right column) orbit as if observed by the Kepler space telescope. The following parameters were used: $P = 1$ year, $\varpi = 0$, $M_{\rm pulsating} = 1.8\ M_\odot$ and $M_{\rm companion} = 0.1\ M_\odot$. This leads to a semi-amplitude of around 34 seconds in the circular case (using Equation 15) and around 15 seconds in the eccentric case (using Equation 17). *Upper panel:* Simulated time delay plot. *Lower panel:* Fourier transformation of the Time Delays. One clearly sees the relative increase of the first harmonic at 2 cycles/year for the eccentric case.

The larger the ratio between the orbital size $a_1 \sin i/c$ and the pulsation period $1/\nu$, the higher is the sensitivity of the method (Murphy et al. 2016b).

Due to the size of the segments, one has to make a trade-off between time or frequency resolution: using a shorter segment size has the advantage of having a finer sensitivity at periastron however the uncertainties are simultaneously increased because of a poorer frequency resolution in the Fourier transform.

Under the assumption of Gaussian noise, increasing the cadence of an observation by an factor of N decreases the uncertainties in the measured phases by a factor of $\sqrt{N}$ (Murphy 2012). The phase errors also scale inversely with amplitude which means that the most valuable frequencies are the ones with the highest amplitudes.

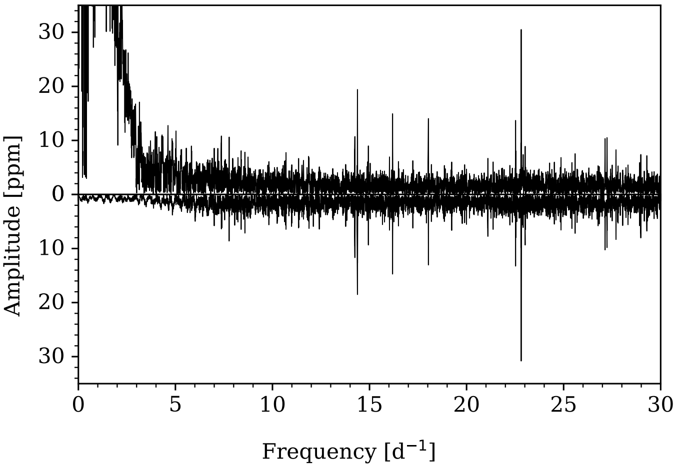

Fig. 4. A comparison of the amplitude spectra of the "raw" PDCSAP light curve (upper panel) and the Gaussian highpass filtered light curve (lower panel). The power of the peaks below 5 d^{-1} are significantly weakened without influencing the δ Scuti pulsations.

4.6. Intrinsic Amplitude and Phase variations

Amplitude modulations in δ Scuti stars have been observed in the past and thoroughly analysed in the four year main Kepler data by Bowman et al. (2016). Additionally due to intrinsic reasons for those modulations (like coupling of pulsational modes or pairs of close unresolved frequencies leading to a beating effect), binarity can cause variability.

β Pictoris is known to show amplitude variation in certain pulsational frequencies as reported by Zwintz et al. (2019) and Mékarnia et al. (2017), however phase modulations were not observed yet (Zwintz et al. 2019).

4.7. Light curve reduction

Following Murphy et al. (2016a), unused frequencies are prewhitened from our light curves as their presence adds unwanted variance to the data. Furthermore, a highpass filter was applied to the light curve to remove any remaining instrumental signal and low frequency oscillations, preserving all content at frequencies above 5 d^{-1}. The effect of a highpass filter on low frequencies can be seen in Figure 4.

5. Results

In order to track the phase modulation over all datasets we start by determining which frequencies do have a signal to noise ratio greater than four in all observations. This is true for the four strongest frequencies in the TESS data (the first four frequencies listed in Table A.1). The stability of those frequencies over the different observations will be analysed in Section 5.1. We will then have a look at time delay curves created from simulated light curves. For this the "best-case scenario" of a four-year Kepler observation of β Pictoris will be studied in Section 5.1.1. The time delays of the real observations and a comparison to a simulated recreation can be found in Section 5.2. Finally, we analyze the pulsational stability of the δ Scuti pulsations of β Pictoris using TESS data in Section 5.3.

5.1. Frequency stability between the different observations

As mentioned in Section 4.5, the PM method derives a time delay from the observed phase modulation at fixed frequencies. The precision with which pulsational frequencies can be determined depends on the quality of the data (cadence, timebase, precision, etc.). The photometry collected by the TESS mission has the smallest uncertainties in frequency of all datasets (see Fig. 5). We therefore use TESS as a "gold standard" for the frequencies which are used in the PM method. The uncertainties in the frequencies were calculated following Montgomery & Odonoghue (1999). As noted in their publication, these errors are however a lower limit of the true values. Keeping in mind that the actual errorbars are probably bigger, one sees that the frequencies are in agreement with each other over the different datasets (Fig. 5).

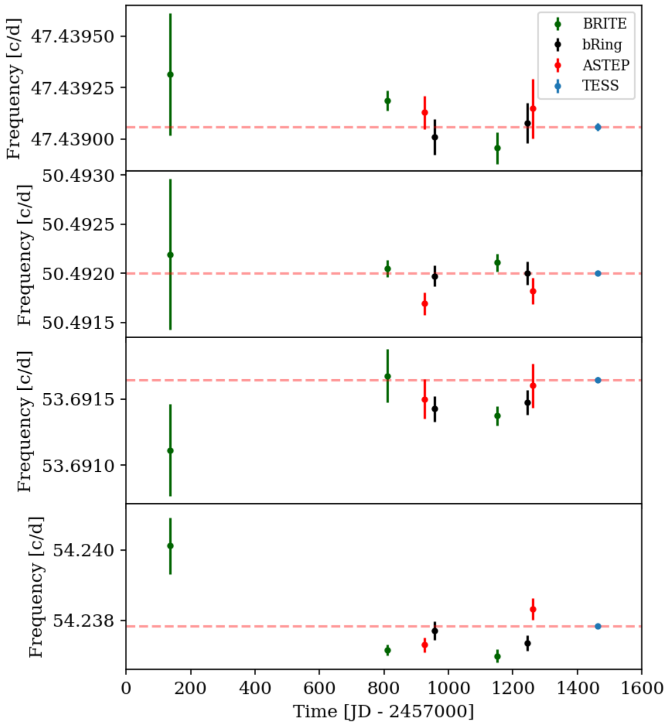

Fig. 5. Frequencies and their uncertainties over all datasets for the four modes which are visible in all observations of the four different observatories. The dashed red line marks the frequency determined by the TESS mission which has the smallest uncertainties. The uncertainties were calculated following Montgomery & Odonoghue (1999).

5.1.1. Simulation

Figure 6 shows the expected time delays for β Pictoris caused by β Pictoris b and β Pictoris c using the full orbital solution given in Table 2. The addition of the individual contributions on the phases gives the total time delay curve as seen by the solid line in Figure 6.

In order to see how properties like photometric precision, cadence and gaps in the observations influence the derived time delays, we simulate light curves of β Pictoris. We use the actual time stamps of the Short Cadence observations of Kepler (Borucki et al. 2010) which have a cadence of around one minute. The simulations consist of a multi-sine of the frequencies listed in Table A.1. Using even more frequencies increases the computational time, without influencing the results of the simulations due to their low amplitudes. The timestamps were then modulated by the expected time delay at a given time using Equation 3 assuming a two planet configuration in this system. Furthermore, Gaussian noise on the order of 30 ppm was added to every data point which is comparable to the noise floor of TESS. Following the procedure explained in Section 4.5, the light curve was separated into 20-day segments and the time delays were calculated from the phases in every segment with a fixed frequency. Finally we calculate weighted time delay values and their corresponding uncertainties using the first three frequencies which have the highest amplitudes.

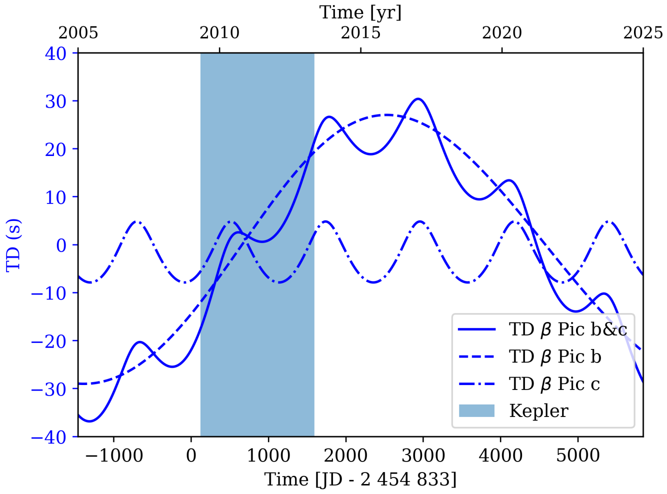

Fig. 6. The expected time delays for two planets in the β Pictoris system (β Pictoris b: dashed line; β Pictoris c: dashed dotted line; both: solid line). The blue shaded region marks the time span of Kepler's four year main mission - note that Kepler did not observe β Pictoris.

The first simulation (Fig. 7) uses the Kepler short cadence, one-minute time stamps. The measured time delays follow the prediction for a two planet case. Removing every second data point, effectively reducing the number of measurements by 50%, does not change the result (Fig. 8). One can, however, observe a small increase in the uncertainties for the time delays. This is expected as a decrease of datapoints by a factor of two increases the uncertainty by a factor of $\sqrt{2}$ assuming Gaussian noise (Murphy 2012). Finally, we induce gaps into the light curve effectively simulating ground based observations by having data only for half of the day. Due to a worse spectral window there are way more peaks present in the amplitude spectrum. These new peaks influence the phases for the observed frequencies as they cannot be resolved anymore. The scatter in the time delays increases significantly (Fig. 9) and one cannot conclusively distinguish between a one planet solution (only β Pictoris b) or a two planet solution. A bigger segment size mitigates this effect as expected by the Rayleigh criterion.

This illustrates clearly that gaps influence the time delays the strongest as the uncertainties in phase only scales with the square root of the cadence factor. One should also remove identified frequencies which are not used in the time delay analysis to get rid of their aliases.

5.2. Time delay analysis of the photometry

Figure 10 shows the predicted time delays caused by the planets in the β Pictoris system during the times when the observatories BRITE, ASTEP, bRing and TESS collected photometry for the

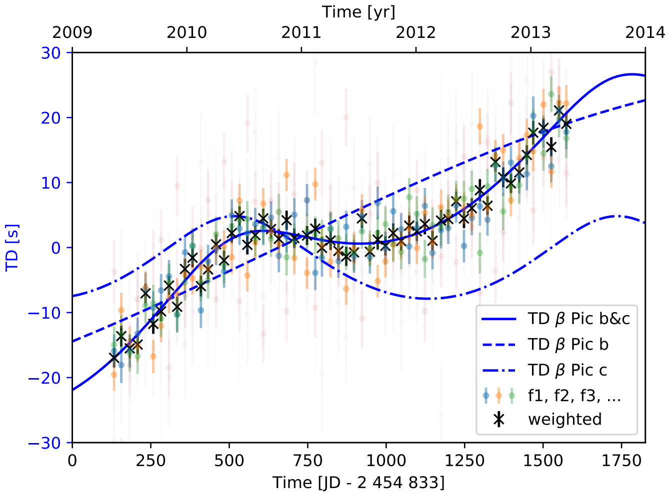

Fig. 7. Derived time delay curve using 20 day segments by simulating Kepler observations of β Pictoris. Properties of the simulated light curve: 1-minute cadence, continuous observations, 20 ppm noise in flux. The strongest frequencies (f1, f2, f3, ..) are shown here with their uncertainties. The weighted average of the measurements is shown in back.

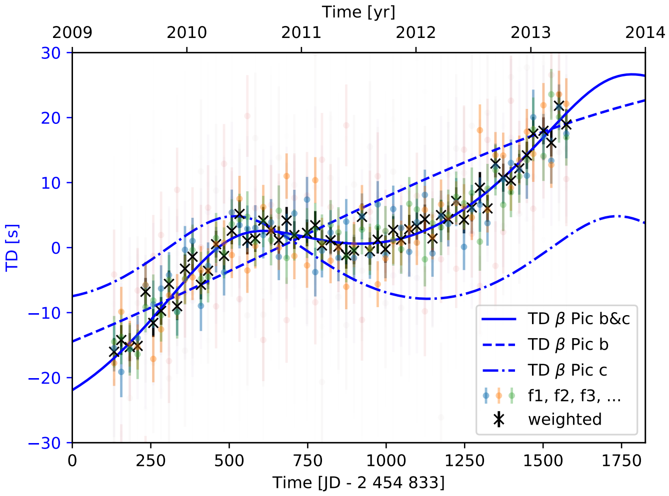

Fig. 8. Derived time delay curve using 20 day segments by simulating Kepler observations of β Pictoris. Properties of the simulated light curve: 2-minute cadence, continuous observations, 20 ppm noise in flux.

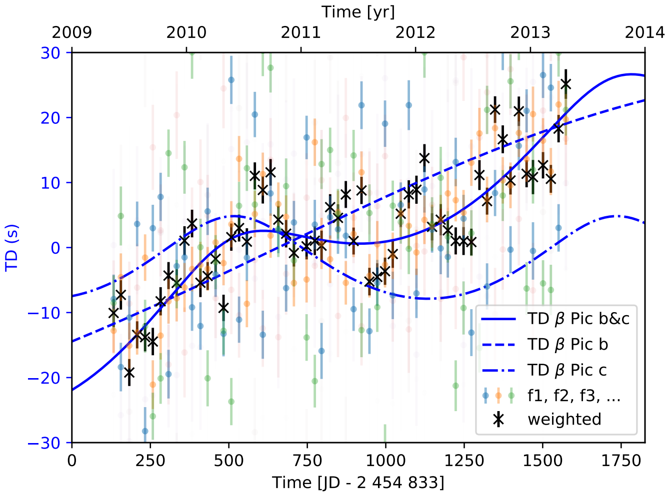

Fig. 9. Derived time delay curve using 20 day segments by simulating Kepler observations of β Pictoris. Properties of the simulated light curve: 1-minute cadence, 0.5-day gaps every day, 20 ppm noise in flux.

star. The available observations have been introduced in Section 3. The semi-amplitude of the predicted time delays for β Pictoris b and c is around 24 and 6 seconds, respectively.

As seen in Section 5.1, the TESS observations show the smallest uncertainties in frequency and are therefore used as a "gold standard" in this analysis. The frequency will be thus fixed to the TESS values, as the phase modulation method observes the phase shifts at a constant frequency (see Section 4.5). The time delays predictions (blue lines in Figure 10, 11 and 12) were also normalized to the midpoint time of TESS. As a time delay is a relative measure and not an absolute one, we set the time delay for TESS to zero. The evaluated time delays shown in Figure 11 and 12 are therefore relative to the TESS values.

A code, which was used to calculate the time delays, was written for this analysis and is heavily based on existing ones, namely `timedelay`[6] and `maelstrom`[7] (Hey et al. 2020). The equations needed to evaluate the time delays are given in Section 4.4 and 4.5.

The phases were calculated by subtracting the midpoint time of the full data set. As discussed in Section 5.1, there are only four frequencies which are significant in all observations. The phases for each data set were then calculated by a least-squares routine and their uncertainties from the respective co-variance matrices. Equation 13 gives us the conversion between the phase of a frequency and respective time delays.

Figure 11 shows the derived time delays for the four different frequencies. They are clearly not consistent with each other. As discussed in Section 4.6, this rules out an extrinsic cause for the modulations like a companion, where all frequencies would show a similar behaviour (examples of this are shown in Figure 3, 7, 8 and 9). A change in frequency was ruled out in Section 5.1. Zwintz et al. (2019) furthermore showed no significant phase change for our four frequencies in the BHr 2018 data set (these four frequencies have the designations F8, F11, F13 and F15 therein).

Next, we try to reproduce the different data sets as close as possible and compare them with the time delay values shown in Figure 11. For that, we first determine frequency, amplitude and phase of the four pulsation modes visible in all observations. We calculate the residual noise for the pre-whitened data sets, which is then used to estimate the uncertainties following Montgomery & Odonoghue (1999). As before, we fix the frequency to the TESS value. As we do not know the exact "true" frequency of the pulsations with infinite precision, we introduce an offset between the true pulsational frequencies and the TESS data set in the simulations. The uncertainty in frequency for these four strongest frequencies are in the order of 10^{-5} d^{-1} (see Table A.1). This offset explains the linear trend for every frequency which is clearly visible in Figure 11. The time delays of the simulated data set is shown in Figure 12.

This linear trend was discussed on simulated data in Section 3.2 of Murphy et al. (2016b) and "almost certainly" explains the

---

[6] https://github.com/danhey/timedelay

[7] https://github.com/danhey/maelstrom

observed trend in the WASP data of Murphy et al. (2013). A way to correct for it is to evaluate the slope between two maxima or minima of the sinusoidal variations. This is not a possibility in our case as we would have to further segment the data sets to identify the position of the maxima or minima, leading to even higher scatter in phase. The lower panel of Figure 11 also shows that the uncertainties in the derived time delays for the datasets other than TESS, are too big to differentiate between a one planet or two planet scenario even without this linear trend. We therefore discuss the possibility of a second β Pictoris observation by TESS in the extended mission in the next section.

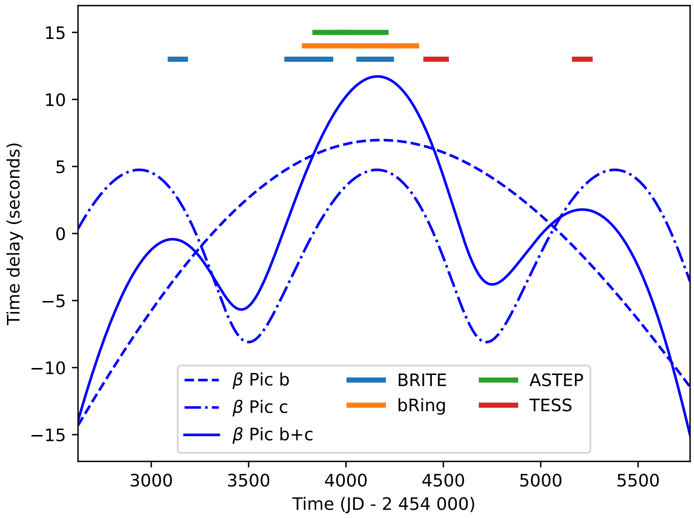

Fig. 10. Time delay predictions for β Pictoris b (dashed line), c (dashed-dotted line) and both planets (solid line). Times when the star was observed are marked with lines.

5.3. Analysis of pulsational stability using TESS data

β Pictoris was observed in seven individual sectors between October 2018 and February 2021 (see Table 3). We performed a frequency analysis of these TESS sectors using `maelstrom`. We find that β Pictoris is seeming undergoing significant frequency and amplitude modulation which buries any signal induced by planetary companions. The periodograms of the stellar pulsations clearly show significant amplitude modulation by the rotational signal (see Fig. 13). We also find that the star is showing modes which are appearing and disappearing on short timescales. Figure 14 shows a mode that seems to be just appearing during the second half of the TESS observations. In summary, we find that β Pictoris' modes are not stable enough to probe to the necessary phase precision for the planetary companions.

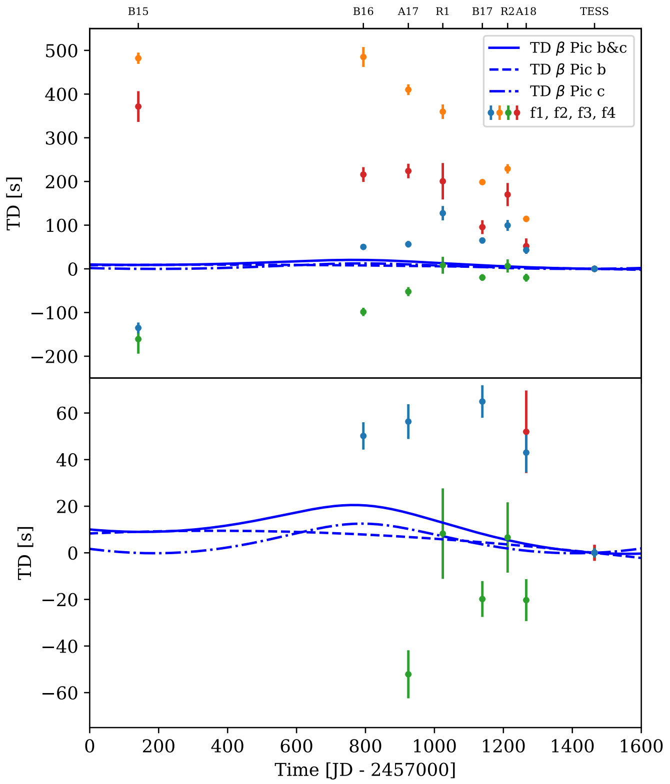

Fig. 11. Time delay plot calculated from the phases of four different frequencies (a color represents a frequency (f1, f2, f3 and f4) listed in Table A.1) for all available observations by BRITE, bRing, ASTEP and TESS. The blue lines indicate time delay predictions for β Pictoris b (dashed line), c (dashed, dotted line) and both planets (solid line). The lower panel is a zoom-in of the upper panel. The uncertainties in the time delays are derived from the co-variance matrices given by the least-squares procedure which was used in order to calculate the phases of the respective frequencies. The ticks at top of the plot denote the various observatories: B15, B16 and B17 for the BRITE observations in the years 2015, 2016 and 2017 respectively, A17 and A18 for the ASTEP observations in 2017 and 2018 and R1 and R2 for the first and second part of the bRing data.

6. Conclusions

In this work, we have analysed the time delays derived from the phases of the δ Scuti pulsations of β Pictoris. The photometric data of the star were collected over a time period of approximately four years by four different observatories: the BRITE-constellation, bRing, ASTEP and TESS. In contrast to previous studies we did not segment the observations in smaller sets (e.g. 10-day bins). This would have caused high uncertainties in the phases and therefore also in the time delays. Either way, we cannot see the influence of β Pictoris b or c in the data due to this scatter. The uncertainty in frequency leads to a linear trend in the time delays which also has been seen in a previous study by Murphy et al. (2013) and in simulations by Murphy et al. (2016b). We furthermore perform a frequency analysis using the open-source tool `maelstrom`. We find that β Pictoris does not have the needed stability to detect planetary companions using the time delay method. The stellar pulsations clearly show strong amplitude modulation caused by the rotational signal and identify modes that are seemingly appearing during our observations.

Previous studies have used the Phase Modulation (PM) method to Kepler data, finding many binary star systems (Mur-

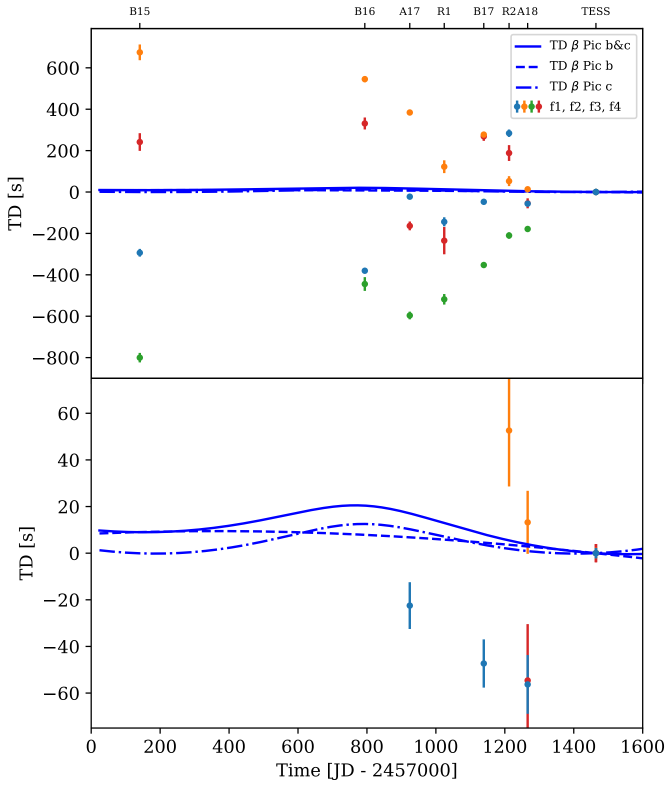

Fig. 12. Time delay plot for the simulated data set showing a high similarity to the time delays of the real data set presented in Figure 12. The colored points represent the simulated time delays for the four strongest pulsational frequencies. The blue lines indicate time delay predictions for β Pictoris b (dashed line), c (dashed-dotted line) and both planets (solid line). The lower panel is a zoom-in of the upper panel. A description for the ticks at top of the plot can be found in the caption of Figure 11.

phy et al. 2016b, ; and references therein) and a planet (Murphy et al. 2016a). This work was the first to use the PM method with so many different data sets that have a precision significantly lower than the Kepler mission. It however remains a valuable method as it is able to find planets and stars in a parameter space which is poorly covered by other methods like the radial velocity method (see e.g. Murphy 2018).

Acknowledgements. This work includes data collected by the TESS mission, which are publicly available from the Mikulski Archive for Space Telescopes (MAST). Funding for the TESS mission is provided by the NASA Explorer Program. This work has made use of data from the European Space Agency (ESA) mission *Gaia* (`https://www.cosmos.esa.int/gaia`), processed by the *Gaia* Data Processing and Analysis Consortium (DPAC, `https://www.cosmos.esa.int/web/gaia/dpac/consortium`). Funding for the DPAC has been provided by national institutions, in particular the institutions participating in the *Gaia* Multilateral Agreement. We made use of the software package `Period04` (Lenz & Breger 2005), the Python programming language (Rossum 1995), and the open-source Python packages `numpy` (van der Walt et al. 2011), `matplotlib` (Hunter 2007), `astropy` (Astropy Collaboration et al. 2013), `lightkurve` (Lightkurve Collaboration et al. 2018), `timedelay`[8], `maelstrom`[9] and `SMURFS` (Müllner 2020). This research has made use of the SIMBAD database, operated at CDS, Strasbourg, France. This research has made use of the NASA Exoplanet Archive, which is operated by the California Institute of Technology, under contract with the National Aeronautics and Space Administration under the Exoplanet Exploration Program. Part of this research was carried out at the Jet Propulsion Laboratory, California Institute of Technology, under a contract with the National Aeronautics and Space Administration (80NM0018D0004). This research has made use of data collected by the BRITE Constellation satellite mission, designed, built, launched, operated and supported by the Austrian Research Promotion Agency (FFG), the University of Vienna, the Technical University of Graz, the University of Innsbruck, the Canadian Space Agency (CSA), the University of Toronto Institute for Aerospace Studies (UTIAS), the Foundation for Polish Science & Technology (FNiTP MNiSW), and National Science Centre (NCN). The bRing observatory at Siding Springs, Australia was supported by a University of Rochester University Research Award. The field activities at Dome C for ASTEP benefit from the support of the French and Italian polar agencies IPEV and PNRA in the framework of the Concordia station programme. The PicSat team thanks funding from the European Research Council (ERC) under the Horizon 2020 research and innovation programme (Grant agreement No. 639248, LITHIUM). SJM was supported by the Australian Research Council (ARC) through Future Fellowship FT210100485.

References

Abe, L., Gonçalves, I., Agabi, A., et al. 2013, A&A, 553, A49
Aerts, C., Christensen-Dalsgaard, J., & Kurtz, D. W. 2010, Asteroseismology
Antoci, V., Cunha, M., Houdek, G., et al. 2014, ApJ, 796, 118
Astropy Collaboration, Robitaille, T. P., Tollerud, E. J., et al. 2013, A&A, 558, A33
Augereau, J. C., Nelson, R. P., Lagrange, A. M., Papaloizou, J. C. B., & Mouillet, D. 2001, A&A, 370, 447
Aumann, H. H., Gillett, F. C., Beichman, C. A., et al. 1984, ApJ, 278, L23
Balona, L. A. 2014, MNRAS, 443, 1946
Barnes, T. G., I. & Moffett, T. J. 1975, AJ, 80, 48
Beust, H. & Morbidelli, A. 2000, Icarus, 143, 170
Blunt, S., Wang, J. J., Angelo, I., et al. 2020, AJ, 159, 89
Borucki, W. J., Koch, D., Basri, G., et al. 2010, Science, 327, 977
Bowman, D. M., Kurtz, D. W., Breger, M., Murphy, S. J., & Holdsworth, D. L. 2016, MNRAS, 460, 1970
Breger, M. & Montgomery, M. H. 2014, ApJ, 783, 89
Breger, M., Stich, J., Garrido, R., et al. 1993, A&A, 271, 482
Compton, D. L., Bedding, T. R., Murphy, S. J., & Stello, D. 2016, MNRAS, 461, 1943
Cousins, A. W. J. 1971, Royal Observatory Annals, 7
Derekas, A., Murphy, S. J., Dálya, G., et al. 2019, MNRAS, 486, 2129
Ferlet, R., Hobbs, L. M., & Madjar, A. V. 1987, A&A, 185, 267
Gaia Collaboration, Prusti, T., de Bruijne, J. H. J., et al. 2016, A&A, 595, A1
Gaia Collaboration, Vallenari, A., Brown, A. G. A., et al. 2023, A&A, 674, A1
Galland, F., Lagrange, A. M., Udry, S., et al. 2006, A&A, 447, 355
Gray, R. O., Corbally, C. J., Garrison, R. F., et al. 2006, AJ, 132, 161
Guillot, T., Abe, L., Agabi, A., et al. 2015, Astronomische Nachrichten, 336, 638
Hermes, J. J. 2018, Timing by Stellar Pulsations as an Exoplanet Discovery Method, 6
Hey, D., Murphy, S., Foreman-Mackey, D., et al. 2020, The Journal of Open Source Software, 5, 2125
Hogg, D. W., Bovy, J., & Lang, D. 2010, arXiv e-prints, arXiv:1008.4686
Houdek, G. 2000, in Astronomical Society of the Pacific Conference Series, Vol. 210, Delta Scuti and Related Stars, ed. M. Breger & M. Montgomery, 454
Hunter, J. D. 2007, Computing in Science and Engineering, 9, 90
Jenkins, J. M. 2017, Kepler Data Processing Handbook: Overview of the Science Operations Center, Tech. rep., NASA Ames Research Center
Jenkins, J. M., Caldwell, D. A., Chandrasekaran, H., et al. 2010, ApJ, 713, L87
Jenkins, J. M., Twicken, J. D., McCauliff, S., et al. 2016, in Society of Photo-Optical Instrumentation Engineers (SPIE) Conference Series, Vol. 9913, Software and Cyberinfrastructure for Astronomy IV, 99133E
Kalas, P., Zwintz, K., Kenworthy, M., et al. 2019, in American Astronomical Society Meeting Abstracts, Vol. 233, American Astronomical Society Meeting Abstracts #233, 218.03
Kanodia, S. & Wright, J. T. 2018, Barycorrpy: Barycentric velocity calculation and leap second management
Kenworthy, M. 2017, Nature Astronomy, 1, 0099
Kenworthy, M. A., Mellon, S. N., Bailey, J. I., et al. 2021, A&A, 648, A15
Koen, C. 2003, MNRAS, 341, 1385
Koen, C. 2014, MNRAS, 444, 1486
Kurtz, D. W., Hambleton, K. M., Shibahashi, H., Murphy, S. J., & Prša, A. 2015, MNRAS, 446, 1223
Lacour, S., Wang, J. J., Rodet, L., et al. 2021, A&A, 654, L2
Lagrange, A. M., Backman, D. E., & Artymowicz, P. 2000, in Protostars and Planets IV, ed. V. Mannings, A. P. Boss, & S. S. Russell, 639
Lagrange, A. M., Boccaletti, A., Langlois, M., et al. 2019a, A&A, 621, L8
Lagrange, A. M., Bonnefoy, M., Chauvin, G., et al. 2010, Science, 329, 57
Lagrange, A. M., De Bondt, K., Meunier, N., et al. 2012, A&A, 542, A18
Lagrange, A. M., Desort, M., Galland, F., Udry, S., & Mayor, M. 2009a, A&A, 495, 335
Lagrange, A. M., Gratadour, D., Chauvin, G., et al. 2009b, A&A, 493, L21

---

[8] `https://github.com/danhey/timedelay`
[9] `https://github.com/danhey/maelstrom`

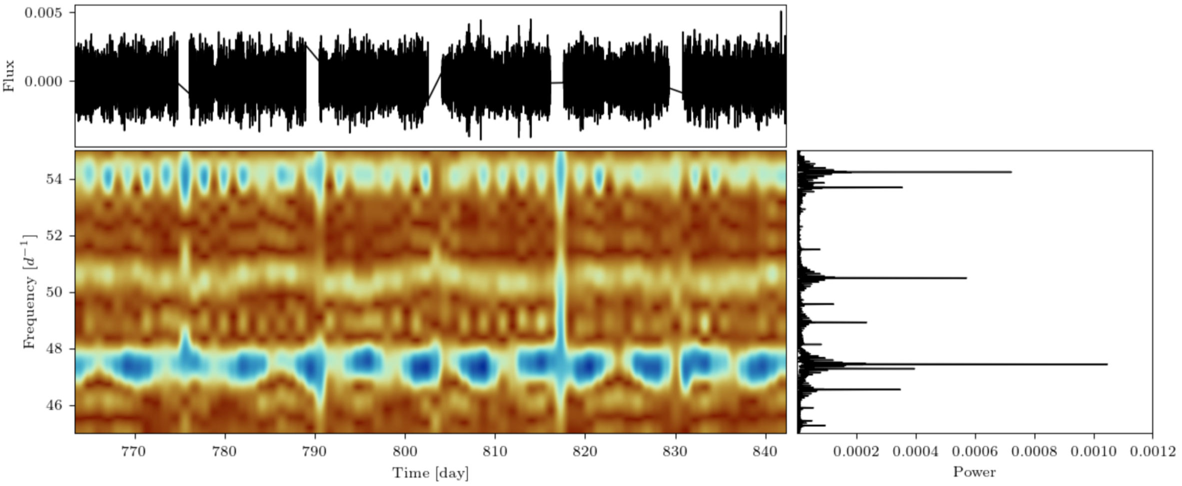

Fig. 13. 2D periodogram showing the frequency region between 45 and 55 d^{-1}. One can see that most of the modes are significantly amplitude modulated by the rotational signal. The mode at 54^{-1} is going much faster, which is probably due to beating with nearby modes. The mode at 50.5^{-1} is itself undergoing incoherent frequency modulation.

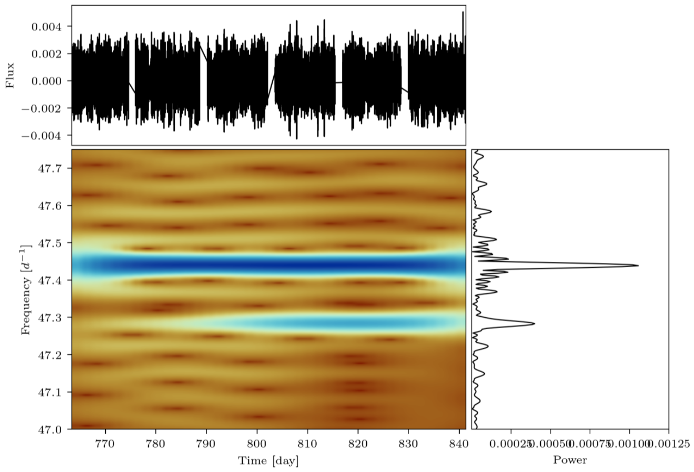

Fig. 14. Periodogram showing a pulsational mode around 47.3 cpd that is just appearing at the end of the observations.

Lagrange, A. M., Meunier, N., Rubini, P., et al. 2019b, Nature Astronomy, 421

Lagrange, A.-M., Rubini, P., Nowak, M., et al. 2020, A&A

Lecavelier Des Etangs, A., Deleuil, M., Vidal-Madjar, A., et al. 1995, A&A, 299, 557

Lecavelier des Etangs, A. & Vidal-Madjar, A. 2016, A&A, 588, A60

Lenz, P. & Breger, M. 2005, Communications in Asteroseismology, 146, 53

Lightkurve Collaboration, Cardoso, J. V. d. M. a., Hedges, C., et al. 2018, Lightkurve: Kepler and TESS time series analysis in Python

Lindegren, L., Klioner, S. A., Hernández, J., et al. 2021, A&A, 649, A2

Lomb, N. R. 1976, Astrophysics and Space Science, 39, 447

Mamajek, E. E. & Bell, C. P. M. 2014, MNRAS, 445, 2169

Mékarnia, D., Chapellier, E., Guillot, T., et al. 2017, A&A, 608, L6

Mellon, S. N., Mamajek, E. E., Stuik, R., et al. 2019, ApJS, 244, 15

Menegaldo, C. G., de O. Fialho, F., Janot-Pacheco, E., Pait, F. M., & Lapeyrère, V. 2022, PASP, 134, 034501

Montgomery, M. H. & Odonoghue, D. 1999, Delta Scuti Star Newsletter, 13, 28

Mouillet, D., Larwood, J. D., Papaloizou, J. C. B., & Lagrange, A. M. 1997, MNRAS, 292, 896

Murphy, S. J. 2012, MNRAS, 422, 665

Murphy, S. J. 2018, arXiv e-prints, arXiv:1811.12659

Murphy, S. J., Bedding, T. R., & Shibahashi, H. 2016a, ApJ, 827, L17

Murphy, S. J., Bedding, T. R., Shibahashi, H., Kurtz, D. W., & Kjeldsen, H. 2014, MNRAS, 441, 2515

Murphy, S. J., Joyce, M., Bedding, T. R., White, T. R., & Kama, M. 2021, MNRAS, 502, 1633

Murphy, S. J., Moe, M., Kurtz, D. W., et al. 2018, MNRAS, 474, 4322

Murphy, S. J., Pigulski, A., Kurtz, D. W., et al. 2013, MNRAS, 432, 2284

Murphy, S. J., Saio, H., Takada-Hidai, M., et al. 2020, MNRAS, 498, 4272

Murphy, S. J. & Shibahashi, H. 2015, MNRAS, 450, 4475

Murphy, S. J., Shibahashi, H., & Bedding, T. R. 2016b, MNRAS, 461, 4215

Müllner, M. 2020, MarcoMuellner/SMURFS 1.1.3

Nesvold, E. R. & Kuchner, M. J. 2015, ApJ, 798, 83

Nowak, M., Lacour, S., Crouzier, A., et al. 2018, in Society of Photo-Optical Instrumentation Engineers (SPIE) Conference Series, Vol. 10698, Space Telescopes and Instrumentation 2018: Optical, Infrared, and Millimeter Wave, ed. M. Lystrup, H. A. MacEwen, G. G. Fazio, N. Batalha, N. Siegler, & E. C. Tong, 1069821

Nowak, M., Lacour, S., Lagrange, A.-M., et al. 2020, A&A

Popowicz, A., Pigulski, A., Bernacki, K., et al. 2017, A&A, 605, A26

Ricker, G. R., Winn, J. N., Vanderspek, R., et al. 2015, Journal of Astronomical Telescopes, Instruments, and Systems, 1, 014003

Rossum, G. 1995, Python Reference Manual, Tech. rep., Centrum voor Wiskunde en Informatica (CWI), Amsterdam, The Netherlands, The Netherlands

Scargle, J. D. 1982, ApJ, 263, 835

Schmid, V. S., Tkachenko, A., Aerts, C., et al. 2015, A&A, 584, A35

Shibahashi, H. & Kurtz, D. W. 2012, MNRAS, 422, 738

Shibahashi, H., Kurtz, D. W., & Murphy, S. J. 2015, MNRAS, 450, 3999

Silvotti, R., Schuh, S., Janulis, R., et al. 2007, Nature, 449, 189

Smart, W. M. 1977, Textbook on Spherical Astronomy, 6th edn. (Cambridge University Press)

Smith, B. A. & Terrile, R. J. 1984, Science, 226, 1421

Smith, J. C., Stumpe, M. C., Van Cleve, J. E., et al. 2012, Publications of the Astronomical Society of the Pacific, 124, 1000

Snellen, I. A. G., Stuik, R., Navarro, R., et al. 2012, in Society of Photo-Optical Instrumentation Engineers (SPIE) Conference Series, Vol. 8444, Proc. SPIE, 84440I

Stassun, K. G., Oelkers, R. J., Paegert, M., et al. 2019, arXiv e-prints, arXiv:1905.10694

Steindl, T., Zwintz, K., & Müllner, M. 2022, A&A, 664, A32

Sterken, C. 2005, in Astronomical Society of the Pacific Conference Series, Vol. 335, The Light-Time Effect in Astrophysics: Causes and cures of the O-C diagram, ed. C. Sterken, 3

Stuik, R., Bailey, J. I., Dorval, P., et al. 2017, A&A, 607, A45

Stumpe, M. C., Smith, J. C., Van Cleve, J. E., et al. 2012, Publications of the Astronomical Society of the Pacific, 124, 985

Talens, G. J. J., Albrecht, S., Spronck, J. F. P., et al. 2017, A&A, 606, A73

Talens, G. J. J., Deul, E. R., Stuik, R., et al. 2018, A&A, 619, A154

van der Walt, S., Colbert, S. C., & Varoquaux, G. 2011, Computing in Science and Engineering, 13, 22

Wang, J. J., Graham, J. R., Pueyo, L., et al. 2016, AJ, 152, 97

Weiss, W. W., Rucinski, S. M., Moffat, A. F. J., et al. 2014, Publications of the Astronomical Society of the Pacific, 126, 573

Wolszczan, A. 1994, Science, 264, 538

Wolszczan, A. & Frail, D. A. 1992, Nature, 355, 145

Wright, J. T. & Eastman, J. D. 2014, PASP, 126, 838

Zieba, S., Zwintz, K., Kenworthy, M. A., & Kennedy, G. M. 2019, A&A, 625, L13

Zwintz, K., Fossati, L., Ryabchikova, T., et al. 2014, Science, 345, 550

Zwintz, K., Reese, D. R., Neiner, C., et al. 2019, A&A, 627, A28

---

[1] Max-Planck-Institut für Astronomie, Königstuhl 17, D-69117 Heidelberg, Germany
[2] Leiden Observatory, Leiden University, Postbus 9513, 2300 RA Leiden, The Netherlands
[3] Institut für Astro- und Teilchenphysik, Universität Innsbruck, Technikerstraße 25, A-6020 Innsbruck
[4] Institute for Astronomy, University of Hawai'i, Honolulu, HI 96822, USA
[5] Centre for Astrophysics, University of Southern Queensland, Toowoomba, QLD 4350, Australia
[6] Institut für Kommunikationsnetze und Satellitenkommunikation, Technical University Graz, Inffeldgasse 12, A-8010 Graz, Austria
[7] Université Côte d'Azur, Observatoire de la Côte d'Azur, CNRS, Laboratoire Lagrange, France
[8] Italian National Agency for New Technologies, Energy and Sustainable Economic Development (ENEA), via Anguillarese 301, Rome, Italy.
[9] Institut polaire français Paul Émile Victor and Programma Nazionale di Ricerche in Antartide, Concordia Station, Antarctica
[10] Istituto Nazionale di Astrofisica, Osservatorio Astronomico di Cagliari, Italy
[11] Department of Physics & Astronomy, University of Rochester, Rochester, NY 14627, USA
[12] Department of Physics, University of California at Santa Barbara, Santa Barbara, CA 93106, USA
[13] Department of Physics and Astronomy, Astronomy and Space Physics, Uppsala University, 751 20 Uppsala, Sweden
[14] Institut de Recherche sur les Exoplanètes, Département de Physique, Université de Montréal, Montréal, QC H3C 3J7, Canada
[15] unaffiliated
[16] Jet Propulsion Laboratory, California Institute of Technology, 4800 Oak Grove Drive, M/S321-100, Pasadena, CA 91109, USA
[17] LESIA, Observatoire de Paris, Université PSL, CNRS, Sorbonne Université, Université de Paris, 5 place Jules Janssen, 92195 Meudon, France
[18] Research School of Astronomy and Astrophysics, Australian National University, Canberra, ACT 2611, Australia
[19] South African Astronomical Observatory, Observatory Rd, Observatory Cape Town, 7700 Cape Town, South Africa
[20] Department of Astronomy, University of Cape Town, Rondebosch, 7700 Cape Town, South Africa
[21] Astronomy Department, University of California, Berkeley, CA 94720, USA
[22] SETI Institute, Carl Sagan Center, 189 Bernardo Ave., Mountain View CA 94043, USA
[23] Institute of Astrophysics, FORTH, GR-71110 Heraklion, Greece
[24] Center for Interdisciplinary Exploration and Research in Astrophysics (CIERA) and Department of Physics and Astronomy, Northwestern University, Evanston, IL 60208, USA
[25] Johns Hopkins APL, Laurel, MD, USA
[26] Astrophysics Research Centre, Queen's University Belfast, Belfast BT7 1NN, UK
[27] School of Physical Sciences and Centre for Astrophysics & Relativity, Dublin City University, Glasnevin, Dublin 9, Ireland
[28] IPAG, Univ. Grenoble Alpes, CNRS, IPAG, F-38000 Grenoble, France
[29] IMCCE - Observatoire de Paris, 77 Avenue Denfert-Rochereau, F-75014 PARIS
[30] Institut d'Astrophysique de Paris, UMR7095 CNRS, Université Pierre & Marie Curie, 98 bis boulevard Arago, 75014 Paris, France
[31] Institute of Astronomy, Madingley Road, Cambridge CB3 0HA, UK
[32] Department of Physics, University of Warwick, Gibbet Hill Road, Coventry CV4 7AL, UK
[33] Centre for Exoplanets and Habitability, University of Warwick, Gibbet Hill Road, Coventry CV4 7AL, UK
[34] Shanghai Observatory, Chinese Academy of Sciences, PR China
[35] Purple Mountain Observatory, Chinese Academy of Science, Nanjing 210008, PR China

Appendix A: TESS frequency analysis

Appendix A.1: Frequency List

Table A.1. Pulsational frequencies, amplitudes in instrumental millimagnitudes (mmag) and normalized flux in parts per million (ppm), phases and signal to noise ratio sorted by the pre-whitening sequence.

#	Freq. (d^{-1})	Ampl. (mmag)	Ampl. (ppm)	Phase	SNR
1	47.43895(6)	1.029(9)	948(9)	0.9071(14)	20.6
2	53.69166(7)	0.948(9)	873(9)	0.2782(16)	19.4
3	50.49168(7)	0.926(9)	852(9)	0.5567(16)	23.4
4	54.23716(12)	0.553(9)	509(9)	0.982(3)	22.8
5	39.06315(15)	0.442(9)	407(9)	0.699(3)	22.5
6	46.54259(16)	0.415(9)	382(9)	0.391(4)	18.7
7	48.9192(3)	0.230(9)	212(9)	0.950(6)	17.3
8	43.5283(3)	0.214(9)	197(9)	0.029(7)	19.9
9	47.2853(4)	0.182(9)	168(9)	0.186(8)	16.2
10	57.4525(4)	0.164(9)	151(9)	0.577(9)	18.0
11	34.7605(5)	0.143(9)	131(9)	0.754(10)	23.7
12	38.1297(5)	0.131(9)	121(9)	0.980(11)	20.2
13	45.2698(5)	0.120(9)	110(9)	0.411(12)	12.8
14	51.4969(6)	0.118(9)	109(9)	0.397(13)	14.7
15	47.2686(7)	0.093(9)	85(9)	0.419(16)	12.3
16	50.8310(8)	0.086(9)	79(9)	0.630(17)	12.9
17	49.7131(8)	0.085(9)	78(9)	0.290(17)	11.3
18	53.8545(8)	0.085(9)	78(9)	0.566(17)	9.5
19	44.6833(8)	0.084(9)	77(9)	0.297(18)	11.3
20	65.1356(8)	0.083(9)	76(9)	0.350(18)	17.9
21	43.8292(8)	0.082(9)	76(9)	0.555(18)	16.3
22	49.5595(8)	0.079(9)	73(9)	0.980(19)	13.4
23	42.0365(9)	0.077(9)	71(9)	0.327(19)	11.1
24	54.2269(9)	0.073(9)	67(9)	0.51(2)	10.0
25	41.6498(9)	0.071(9)	65(9)	0.59(2)	13.0
26	48.1381(10)	0.064(9)	59(9)	0.23(2)	11.2
27	45.8998(10)	0.064(9)	59(9)	0.73(2)	12.4
28	50.2689(12)	0.054(9)	50(9)	0.90(3)	12.1
29	75.6780(13)	0.052(9)	48(9)	0.68(3)	12.2
30	58.3469(13)	0.050(9)	46(9)	0.61(3)	11.3
31	45.4375(14)	0.047(9)	44(9)	0.00(3)	12.3
32	54.4625(14)	0.047(9)	43(9)	0.16(3)	8.1
33	53.6827(15)	0.042(9)	39(9)	0.16(3)	7.3
34	53.5521(16)	0.040(9)	37(9)	0.48(4)	7.7
35	42.1735(16)	0.040(9)	37(9)	0.70(4)	9.5
36	58.2515(17)	0.039(9)	36(9)	0.81(4)	10.5
37	42.3963(17)	0.039(9)	36(9)	0.68(4)	11.5

Appendix A.2: Gaussian highpass filter

By applying a Gaussian high-pass filter on the TESS light curve (see Fig. A.1), the long term variations like systematics and the exocomets are significantly weakened while preserving the higher frequencies related to the δ Scuti pulsations at the same time.

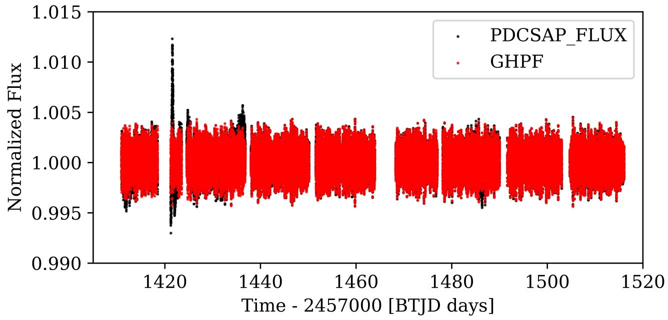

Fig. A.1. A comparison of the PDCSAP light curve (black in the background) and the Gaussian highpass filter (GHPF; red dots) of it. The GHPF clearly shows less long term variations in the light curve.